





Cascaded H-Bridge based Parallel Hybrid Converter - A novel Topology for perfectly sinusoidal high power Voltage Sources


Lukas Stefanski 
Institute of Electrical Engineering
Karlsruhe Institute of Technology (KIT)
Karlsruhe, Germany
lukas.stefanski@kit.edu

Christoph Rollbühler
Institute of Electrical Engineering
Karlsruhe Institute of Technology (KIT)
Karlsruhe, Germany
c.rollbuehler@kit.edu

Daniel Bernet 
Institute of Electrical Engineering
Karlsruhe Institute of Technology (KIT)
Karlsruhe, Germany
daniel.bernet@kit.edu

Andreas Liske 
Institute of Electrical Engineering
Karlsruhe Institute of Technology (KIT)
Karlsruhe, Germany
andreas.liske@kit.edu

Mathias Schnarrenberger 
R&D
AVL SET GmbH
Wangen im Allgäu, Germany
mathias.schnarrenberger@avl.com

Marc Hiller 
Institute of Electrical Engineering
Karlsruhe Institute of Technology (KIT)
Karlsruhe, Germany
marc.hiller@kit.edu

Abstract— The demand for high voltage, high power, high precision and high dynamic 3AC-voltage sources is increasing constantly. One application that gets more and more important in recent years and demands such voltage sources is e.g. Power-Hardware-in-the-Loop (PHIL) Emulation. In this paper a new power converter topology called “Parallel Hybrid Converter” or PHC is presented and a corresponding control scheme is derived. This new converter has a terminal behavior similar to a MMC or MPPMC but compared to them the PHC features significantly reduced costs and a significantly improved power density.

Keywords— Parallel Hybrid Converter (PHC), energy and balancing control, predictive current control, Power-Hardware-in-the-Loop, Cascaded H-Bridge Converter (CHB), Modular Multilevel Converter (MMC)

I. INTRODUCTION

The new “Parallel Hybrid Converter“ (PHC) is based on the concept of Parallel Hybrid Amplifiers (PHA), which were first introduced in [1] and later further investigated in [2–4]. A simplified equivalent circuit diagram of the PHA and the idealized voltage and current waveforms for an ohmic load can be seen in Fig. 1. The basic concept of a PHA is the combination of the very low harmonic output voltage quality of a low power linear amplifier with the high efficiency and high power density of a switching converter. The linear amplifier acts as voltage source and hence defines the output voltage u_o as Correction Unit (CU). The switching converter is used as the Main Power Source (MPS) and provides the bulk of the resulting output current i_o . It is coupled to the CU via an inductor and hence acts as current source. To limit the current of the CU, a hysteresis controller is used to determine the switching states of the MPS. Thus, instead of a single high power, heavy and expensive linear amplifier, a considerably cheaper, more compact and efficient PHA can be used as a universal voltage source.

We adapted this concept to multilevel converters with the goal to increase power density and reduce cost. This led to the new topology of the PHC shown in Fig. 2. It is composed of the parallel arrangement of a conventional high power three phase two level IGBT converter as main power source (MPS) and a

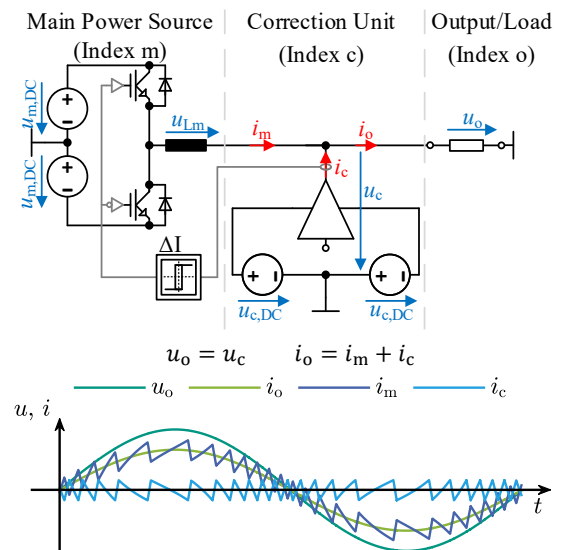


Fig. 1 Simplified schematic of a Parallel Hybrid Amplifier and idealized voltage and current waveforms

three phase low power Cascaded H-Bridge Converter (CHB) in star configuration as correction unit (CU). This new converter topology is perfectly suited to be used as a universal low harmonics sinusoidal voltage source. Hence, it is suitable to replace more complex state-of-the-art multilevel converter topologies such as the Modular Multilevel Converter (MMC) [5] or the Modular Multiphase Multilevel Converter (MPPMC) [6]. The PHC topology is also well suited to replace bulky and expensive LCL-filters in conventional grid-connected converter systems. Therefore, the filter capacitors are replaced by the CU allowing a reduction in inductance of up to 50 % [7]. In medium voltage applications, three or five level converter topologies can be used as MPS instead of a two level converter [8].

In Section II the new PHC is introduced and the basic working principle is explained. The transformed equivalent circuit diagrams required for a decoupled control are derived. Based on this, a power analysis is performed to identify the possible control variables with which the capacitor energies within the CHB cells of the PHC can be controlled. On basis of

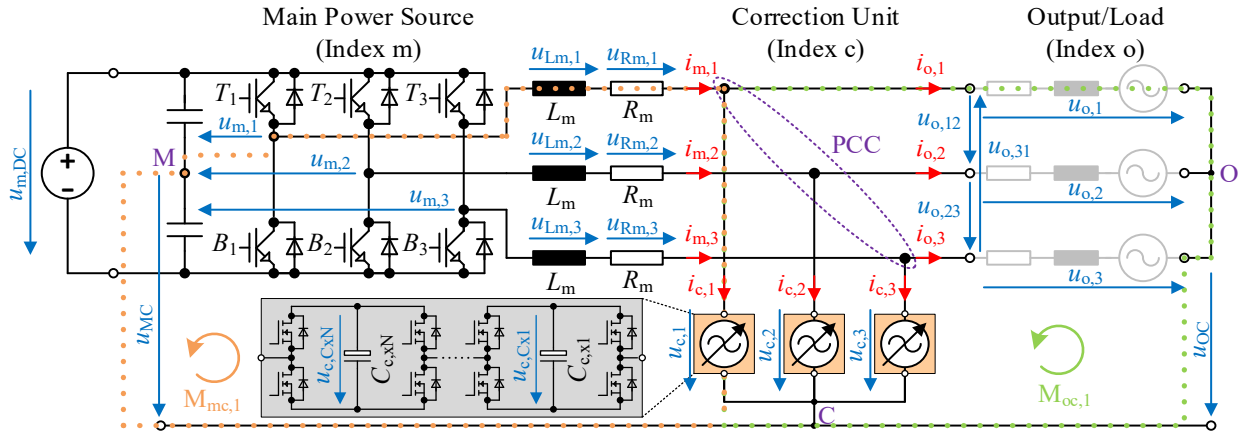


Fig. 2 Detailed equivalent circuit of the novel Parallel Hybrid Converter (PHC)

this, a control scheme for the overall current and energy control of the CU and the MPS is presented in Section III. Simulation results are shown in Section IV. The paper concludes with a summary in Section V.

II. FUNCTIONAL PRINCIPLE OF THE PHC

The circuit diagram of the PHC is shown in Fig. 2. The two level IGBT converter as Main Power Source (MPS) is supplied with power via the DC connection from a DC voltage source. The coupling inductors L_m and their line resistances R_m , connect the MPS to the so called “Point of Common Coupling” (PCC) and change the behavior of the two level converter from a voltage source to a current source. Also connected to the PCC is the multilevel converter based voltage source as Correction Unit (CU). In the grey-boxed area the inner structure of the drawn orange voltage sources is sketched. In this paper a Cascaded H-Bridge Converter (CHB) is used as CU. On the right are the output terminals with an exemplary load. The indexes used throughout this paper are “m” for the values of the MPS, “c” for the values of the CU/CHB and “o” for the output respectively load values.

The basic operating principle of the PHC is based on the idea that a low-power multilevel converter as CU defines the output voltage $u_{o,x}$ and thus the output current $i_{o,x}$, whereas a high-power two level converter as MPS delivers the bulk of the output current $i_{m,x} \approx i_{o,x}$. In order to gain a more detailed understanding of the circuit's operating principle, the mesh and node equations are derived in matrix notation according to Kirchhoff's laws. The meshes $[M_{mc,123}]$ from the MPS to the CU are given in (1) and exemplarily shown for phase 1 in Fig. 2 as an orange dotted line.

$$\begin{bmatrix} u_{m,1} \\ u_{m,2} \\ u_{m,3} \end{bmatrix} = \begin{bmatrix} u_{c,1} \\ u_{c,2} \\ u_{c,3} \end{bmatrix} + R_m \begin{bmatrix} i_{m,1} \\ i_{m,2} \\ i_{m,3} \end{bmatrix} + L_m \frac{d}{dt} \begin{bmatrix} i_{m,1} \\ i_{m,2} \\ i_{m,3} \end{bmatrix} - \begin{bmatrix} u_{MC} \\ u_{MC} \\ u_{MC} \end{bmatrix} \quad (1)$$

The meshes $[M_{oc,123}]$ from the output to the CU are given in (2) and exemplarily shown for phase 1 in Fig. 2 as a green dotted line.

$$\begin{bmatrix} u_{c,1} \\ u_{c,2} \\ u_{c,3} \end{bmatrix} = \begin{bmatrix} u_{o,1} \\ u_{o,2} \\ u_{o,3} \end{bmatrix} + \begin{bmatrix} u_{OC} \\ u_{OC} \\ u_{OC} \end{bmatrix} \quad (2)$$

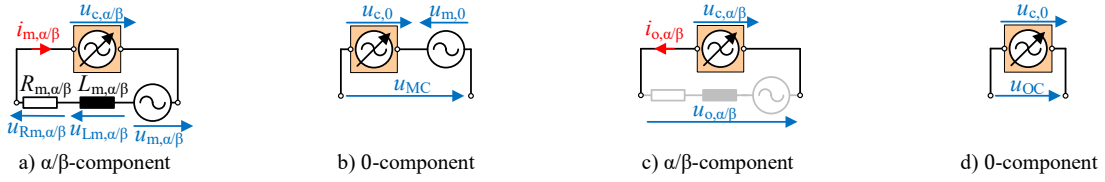
The node equations for the three nodes M, C and O are given in (3) and the node equations for the PCC are given in (4). In Fig. 2 the node labels M, C, O and PCC are in purple. In the following the index $x \in \{1,2,3\}$ defines the phase number.

$$\begin{bmatrix} 0 \\ 0 \\ 0 \end{bmatrix} = \begin{bmatrix} i_{m,1} \\ i_{c,1} \\ i_{o,1} \end{bmatrix} + \begin{bmatrix} i_{m,2} \\ i_{c,2} \\ i_{o,2} \end{bmatrix} + \begin{bmatrix} i_{m,3} \\ i_{c,3} \\ i_{o,3} \end{bmatrix} \quad (3)$$

$$\begin{bmatrix} i_{c,1} \\ i_{c,2} \\ i_{c,3} \end{bmatrix} = \begin{bmatrix} i_{m,1} \\ i_{m,2} \\ i_{m,3} \end{bmatrix} - \begin{bmatrix} i_{o,1} \\ i_{o,2} \\ i_{o,3} \end{bmatrix} \quad (4)$$

As can be seen in (1) the MPS voltages $u_{m,x}$ have no influence on the output voltages $u_{o,x}$ of the PHC. The output voltages $u_{o,x}$ are solely defined by the CU voltages $u_{c,x}$ as the mesh equations in (2) show. Thus the CU defines the output currents $i_{o,x}$ of the PHC independently of the MPS. As long as it can act as a voltage source, which is given if its maximum rated current is not exceeded. The node equations of the PCC in (4) on the other hand show that the CU only has to compensate the differences between the output currents $i_{o,x}$ and the MPS currents $i_{m,x}$. With a proper control of the MPS limiting the CU currents $i_{c,x}$, these differences are reduced to the current ripple of the two level MPS. Thus the CU only has to deliver distortion reactive power. This reactive power is significantly lower in comparison to the output power of the PHC, which is completely delivered by the MPS. Taking this into account a low power multilevel converter with no extra power supply perfectly meets the requirements of a CU. To ensure the ripple currents $i_{c,x}$ have no influence on the output voltages $u_{o,x}$ of the PHC, the CU must have an output impedance close to zero [1]. Because of this, we use a CHB with one arm per phase in star configuration as CU. This type of modular built multilevel converter has the lowest output impedance compared to a CHB in delta configuration, MMCs or MMPMCs.

As can be seen in the grey-boxed area in Fig. 2 each CU/CHB arm has N cells connected in series. Each cell consists of an H-Bridge with a cell capacitor $C_{c,xy}$ and can generate the voltages $0V$, $+u_{c,Cxy}$ and $-u_{c,Cxy}$. Where the cell number is defined by $y \in \{N|1 \leq y \leq N\}$. One CU/CHB phase can generate an output voltage $u_{c,x}$ with $2N + 1$ levels within the range given in (5).



$$[M_{mc,\alpha\beta 0}] = [C][M_{mc,123}]$$

$$[M_{oc,\alpha\beta 0}] = [C][M_{oc,123}]$$

Fig. 3 Equivalent circuit diagrams of the transformed mesh equations $[M_{mc,123}]$ on the left and $[M_{oc,123}]$ on the right

$$-u_{c,Cx} = -\sum_{y=1}^N u_{c,Cxy} \leq u_{c,x} \leq \sum_{y=1}^N u_{c,Cxy} = +u_{c,Cx} \quad (5)$$

The voltage $u_{c,Cx}$ is the arm capacitor voltage of phase x and equals the sum of all cell capacitor voltages $u_{c,Cxy}$ in this arm. The energy $w_{c,x}$ in each CU/CHB arm is calculated with (6).

$$w_{c,x} = \frac{1}{2} C_{c,x} \cdot u_{c,Cx}^2 = \frac{1}{2} \frac{C_{c,xy}}{N} \cdot \left(\sum_{y=1}^N u_{c,Cxy} \right)^2 \quad (6)$$

The CU/CHB has only capacitors and no extra power supply in its cells. Therefore the energy $w_{c,x}$ in each CU/CHB arm only can be influenced by the arm power $p_{c,x} = u_{c,x} i_{c,x}$. According to [9] the energy in an arm can be split into a constant value \bar{w}_c and a time-variant value \tilde{w}_c (see (7)).

$$\begin{bmatrix} w_{c,1} \\ w_{c,2} \\ w_{c,3} \end{bmatrix} = \begin{bmatrix} \bar{w}_c \\ \bar{w}_c \\ \bar{w}_c \end{bmatrix} + \begin{bmatrix} \tilde{w}_{c,1} \\ \tilde{w}_{c,2} \\ \tilde{w}_{c,3} \end{bmatrix} = \begin{bmatrix} \bar{w}_c \\ \bar{w}_c \\ \bar{w}_c \end{bmatrix} + \int \begin{bmatrix} p_{c,1} \\ p_{c,2} \\ p_{c,3} \end{bmatrix} dt \quad (7)$$

To ensure a constant arm energy $w_{c,x}$ and thus ensure a constant arm capacitor voltage $u_{c,Cx}$ the time average value of the arm power $\bar{p}_{c,x}$ has to be kept zero. To do so a decoupled control strategy has to be defined. This control strategy has to compensate the losses within the CU/CHB cells and also has to compensate active power components in the CU/CHB arm powers $p_{c,x}$. Therefore the decoupled equivalent circuit diagrams and their corresponding equations will be derived in Section II.A. Based on this, a power analysis is performed in Section II.B. The analysis is done to identify the possible control variables with which the occurring CU/CHB arm powers $p_{c,x}$ and therefore the CU/CHB arm capacitor energies $w_{c,x}$ can be controlled. This approach is similar to the one used in [5] and [9] to derive a decoupled control schema for the MMC.

A. Calculation of the transformed and decoupled equivalent circuit diagrams

In order to ensure a constant arm energy $w_{c,x}$, a decoupled control strategy has to be defined. Therefore the derived mesh equations $[M_{mc,123}]$ in (1) and $[M_{oc,123}]$ in (2) as well as the derived node equations given in (3) and (4) are transformed into the $\alpha\beta 0$ -system. The transformation is done by using the amplitude invariant Clarke transformation matrix $[C]$ given in (8) and the definitions for the transformed currents, the transformed voltages and transformed common mode voltages given in (9) with the index $z \in \{m, c, o\}$ and the index $Z \in \{M, O\}$.

$$[C] = \frac{2}{3} \begin{bmatrix} 1 & -1/2 & -1/2 \\ 0 & \sqrt{3}/2 & -\sqrt{3}/2 \\ 1/2 & 1/2 & 1/2 \end{bmatrix} \quad (8)$$

$$\begin{bmatrix} i_{z,\alpha} \\ i_{z,\beta} \\ i_{z,0} \end{bmatrix} = [C] \begin{bmatrix} i_{z,1} \\ i_{z,2} \\ i_{z,3} \end{bmatrix}, \begin{bmatrix} u_{z,\alpha} \\ u_{z,\beta} \\ u_{z,0} \end{bmatrix} = [C] \begin{bmatrix} u_{z,1} \\ u_{z,2} \\ u_{z,3} \end{bmatrix}, \begin{bmatrix} 0 \\ 0 \\ u_{zC} \end{bmatrix} = [C] \begin{bmatrix} u_{zC} \\ u_{zC} \\ u_{zC} \end{bmatrix} \quad (9)$$

The node equations resulting from (3) and (4) are given in (10). The common mode currents $i_{z,0}$ cannot occur since the nodes M, C and O are not connected.

$$\begin{bmatrix} i_{c,\alpha} \\ i_{c,\beta} \\ 0 \end{bmatrix} = \begin{bmatrix} i_{m,\alpha} - i_{o,\alpha} \\ i_{m,\beta} - i_{o,\beta} \\ 0 \end{bmatrix} \quad (10)$$

In (11) the mesh equations $[M_{mc,\alpha\beta 0}]$ are depicted. They result from the transformation of the mesh equations $[M_{mc,123}]$ given in (1).

$$\begin{bmatrix} u_{m,\alpha} \\ u_{m,\beta} \\ u_{m,0} \end{bmatrix} = \begin{bmatrix} u_{c,\alpha} \\ u_{c,\beta} \\ u_{c,0} \end{bmatrix} + R_m \begin{bmatrix} i_{m,\alpha} \\ i_{m,\beta} \\ 0 \end{bmatrix} + L_m \frac{d}{dt} \begin{bmatrix} i_{m,\alpha} \\ i_{m,\beta} \\ 0 \end{bmatrix} - \begin{bmatrix} 0 \\ 0 \\ u_{MC} \end{bmatrix} \quad (11)$$

The mesh equations $[M_{oc,\alpha\beta 0}]$ given in (12) result from the transformed mesh equations $[M_{oc,123}]$ given in (2).

$$\begin{bmatrix} u_{c,\alpha} \\ u_{c,\beta} \\ u_{c,0} \end{bmatrix} = \begin{bmatrix} u_{o,\alpha} \\ u_{o,\beta} \\ u_{o,0} \end{bmatrix} + \begin{bmatrix} 0 \\ 0 \\ u_{OC} \end{bmatrix} \Rightarrow \begin{bmatrix} u_{c,\alpha} \\ u_{c,\beta} \\ u_{c,0} \end{bmatrix} = \begin{bmatrix} u_{o,\alpha} \\ u_{o,\beta} \\ u_{o,0} \end{bmatrix} \quad (12)$$

The equivalent circuit diagrams shown in Fig. 3 illustrate the transformed mesh equations (11) and (12). To the left in Fig. 3 a) and b) the $\alpha\beta$ - and the 0-components of the mesh $[M_{mc,\alpha\beta 0}]$ are drawn. Fig. 3 a) shows that the MPS currents $i_{m,\alpha\beta}$ into the CU/CHB can be controlled with the MPS voltages $u_{m,\alpha\beta}$, decoupled from the output currents $i_{o,\alpha\beta}$ of the PHC. Thereby the CU/CHB voltages $u_{c,\alpha\beta}$ respectively the PHC output voltages $u_{o,\alpha\beta}$ (see (12)) occur as disturbance variables. These voltages are determined by the superimposed load control of the application. To the right in Fig. 3 c) and d) the $\alpha\beta$ - and the 0-components of the output mesh $[M_{oc,\alpha\beta 0}]$ are illustrated. Fig. 3 c) shows that the PHC output currents $i_{o,\alpha\beta}$ are directly controllable by the CU/CHB voltages $u_{c,\alpha\beta}$, decoupled from the MPS. Furthermore, Fig. 3 b) and d) show that the common mode voltages $u_{z,0}$ of the MPS, CU/CHB and the output do not have any influence on the MPS, CU/CHB and the output currents $i_{z,\alpha\beta}$. This is due to the unconnected nodes M, C and O. Thus the common mode voltages $u_{z,0}$ are available as degrees of freedom.

B. Analysis of the CU/CHB arm powers

On basis of the decoupled mesh equations we derived in the previous subsection, we perform a power analysis in this subsection. The goal is to find possible control variables (currents and/or voltages) to control the occurring CU/CHB arm powers $p_{c,x}$ and thus the CU/CHB arm capacitor energies $w_{c,x}$.

For the analysis the occurring arm powers $p_{c,x} = i_{c,x}u_{c,x}$ inside the CU/CHB arms are calculated and transformed into the $\alpha\beta 0$ -system using the Clarke transformation matrix [C].

$$\begin{bmatrix} p_{c,\alpha} \\ p_{c,\beta} \\ p_{c,0} \end{bmatrix} = [C] \begin{bmatrix} p_{c,1} \\ p_{c,2} \\ p_{c,3} \end{bmatrix} = \begin{bmatrix} -i_{o,\alpha}u_{c,0} + i_{m,\alpha}u_{c,0} \\ -i_{o,\beta}u_{c,0} + i_{m,\beta}u_{c,0} \\ 0 \end{bmatrix} + \frac{1}{2} \begin{bmatrix} -i_{o,\alpha}u_{o,\alpha} + i_{o,\beta}u_{o,\beta} + i_{m,\alpha}u_{o,\alpha} - i_{m,\beta}u_{o,\beta} \\ +i_{o,\alpha}u_{o,\beta} + i_{o,\beta}u_{o,\alpha} - i_{m,\alpha}u_{o,\beta} - i_{m,\beta}u_{o,\alpha} \\ -i_{o,\alpha}u_{o,\alpha} - i_{o,\beta}u_{o,\beta} + i_{m,\alpha}u_{o,\alpha} + i_{m,\beta}u_{o,\beta} \end{bmatrix} \quad (13)$$

The arm energies $w_{c,x}$ given in (7) are also transformed into the $\alpha\beta 0$ -system and are given in (14). The mean value of the energy in the three CU/CHB arms is given with the energy $w_{c,0}$ and is called ‘‘mean energy’’ in the following. The energy differences between the three arms are given with the energies $w_{c,\alpha}$ and $w_{c,\beta}$ and are called ‘‘difference energies’’ in the following.

$$\begin{bmatrix} w_{c,\alpha} \\ w_{c,\beta} \\ w_{c,0} \end{bmatrix} = [C] \begin{bmatrix} w_{c,1} \\ w_{c,2} \\ w_{c,3} \end{bmatrix} = \begin{bmatrix} 0 \\ 0 \\ \bar{w}_c \end{bmatrix} + \int \begin{bmatrix} p_{c,\alpha} \\ p_{c,\beta} \\ p_{c,0} \end{bmatrix} dt \quad (14)$$

After calculating the transformed arm powers $p_{c,\alpha\beta 0}$ given in (13) they are searched for unique voltage-current combinations which result in active power components ($\int p_{c,\alpha\beta 0} dt \neq 0$). With these active power components the energies $w_{c,\alpha\beta 0}$ in the CU/CHB can be controlled directly (see (14)). As depicted in (14) each power only influences its corresponding energy. The powers $p_{c,\alpha}$ and $p_{c,\beta}$ only cause an energy shift inside the CU/CHB. Thus they could be used to compensate the difference energies $w_{c,\alpha\beta}$ between the three CU/CHB arms. Whereas the power $p_{c,0}$ only causes an even increase or decrease of the mean energy $w_{c,0}$ inside the CU/CHB. As will be shown later the reference values of the active power components $p_{c,0}^*$, $p_{c,\alpha}^*$ and $p_{c,\beta}^*$ are provided by three independent energy controllers one each for the mean energy $w_{c,0}$ and the difference energies $w_{c,\alpha}$ and $w_{c,\beta}$.

For a simplified approach, the voltages and currents for the power analysis are defined as sinusoidal and represented in polar coordinates in (15)-(21). The power analysis is based on ideal voltage sources as depicted in Fig. 3. Thus switching frequency based current ripples are neglected in this approach. Equations (15) and (16) describe the symmetric and sinusoidal output voltage $\underline{u}_o = u_{o,\alpha} + ju_{o,\beta}$ and output current $\underline{i}_o = i_{o,\alpha} + ji_{o,\beta}$ with the output angle $\gamma_o = 2\pi f_o t$ and the phase shift $\varphi_o = \angle \underline{i}_o \underline{u}_o$ between the output voltage \underline{u}_o and the output current \underline{i}_o . The amplitudes are given with \hat{u}_o and \hat{i}_o .

$$\begin{bmatrix} u_{o,\alpha} \\ u_{o,\beta} \end{bmatrix} = \hat{u}_o \begin{bmatrix} \cos(\gamma_o) \\ \sin(\gamma_o) \end{bmatrix} \quad (15)$$

$$\begin{bmatrix} i_{o,\alpha} \\ i_{o,\beta} \end{bmatrix} = \hat{i}_o \begin{bmatrix} \cos(\gamma_o - \varphi_o) \\ \sin(\gamma_o - \varphi_o) \end{bmatrix} \quad (16)$$

The sinusoidal common mode voltage of the CU/CHB $u_{c,0}$ is given in (17) with the amplitude $\hat{u}_{c,0}$ and the angle $\gamma_{c,0} = 2\pi f_{c,0} t$. On the contrary to the output frequency f_o , the frequency $f_{c,0}$ of the CU/CHB common mode voltage $u_{c,0}$ is defined to be not variable and has a fixed value.

$$u_{c,0} = \hat{u}_{c,0} \cos(\gamma_{c,0}) \quad (17)$$

In order to anticipate a part of the solution, it is further defined that the MPS current $\underline{i}_m = i_{m,\alpha} + ji_{m,\beta}$ given in (18) is composed of the three independent sinusoidal current components $\underline{i}_{m,P}$, $\underline{i}_{m,N}$ and $\underline{i}_{m,c,0}$.

$$\begin{bmatrix} i_{m,\alpha} \\ i_{m,\beta} \end{bmatrix} = \begin{bmatrix} i_{m,P,\alpha} \\ i_{m,P,\beta} \end{bmatrix} + \begin{bmatrix} i_{m,N,\alpha} \\ i_{m,N,\beta} \end{bmatrix} + \begin{bmatrix} i_{m,c,0,\alpha} \\ i_{m,c,0,\beta} \end{bmatrix} \quad (18)$$

The current component $\underline{i}_{m,P} = i_{m,P,\alpha} + ji_{m,P,\beta}$ given in (19) is a positive sequence current (index ‘‘P’’ for positive sequence) with the angle $\gamma_o = 2\pi f_o t$, the phase shift $\varphi_o = \angle \underline{i}_{m,P} \underline{u}_o = \angle \underline{i}_o \underline{u}_o$ and the amplitude $\hat{i}_{m,P}$.

$$\begin{bmatrix} i_{m,P,\alpha} \\ i_{m,P,\beta} \end{bmatrix} = \hat{i}_{m,P} \begin{bmatrix} \cos(\gamma_o - \varphi_o) \\ \sin(\gamma_o - \varphi_o) \end{bmatrix} \quad (19)$$

The current component $\underline{i}_{m,N} = i_{m,N,\alpha} + ji_{m,N,\beta}$ given in (20) is a negative sequence current (index ‘‘N’’ for negative sequence) with the angle $\gamma_o = 2\pi f_o t$ of the output voltage \underline{u}_o , the phase shift $\varphi_{o,N} = \angle \underline{i}_{m,N} \underline{u}_o$ and the amplitude $\hat{i}_{m,N}$.

$$\begin{bmatrix} i_{m,N,\alpha} \\ i_{m,N,\beta} \end{bmatrix} = \hat{i}_{m,N} \begin{bmatrix} \cos(-\gamma_o - \varphi_{o,N}) \\ \sin(-\gamma_o - \varphi_{o,N}) \end{bmatrix} \quad (20)$$

The current component $\underline{i}_{m,c,0} = i_{m,c,0,\alpha} + ji_{m,c,0,\beta}$ given in (21) is a positive sequence current with the angle $\gamma_{c,0} = 2\pi f_{c,0} t$ of the CU/CHB common mode voltage $u_{c,0}$, the phase shift $\varphi_{c,0} = \angle \underline{i}_{m,c,0} u_{c,0}$ and the amplitude $\hat{i}_{m,c,0}$.

$$\begin{bmatrix} i_{m,c,0,\alpha} \\ i_{m,c,0,\beta} \end{bmatrix} = \hat{i}_{m,c,0} \begin{bmatrix} \cos(\gamma_{c,0} - \varphi_{c,0}) \\ \sin(\gamma_{c,0} - \varphi_{c,0}) \end{bmatrix} \quad (21)$$

At this point, (15)-(21) are inserted in (13) and presented in Table I for a better overview. The table is structured as follows: Each row contains a unique combination of the causing voltage component u and the causing current component i . The resulting powers are separated into the columns $p_{c,0}$ and $\underline{p}_c = p_{c,\alpha} + jp_{c,\beta}$. Each entry in Table I consists of two elements. The first contains the amplitude of the variable (\hat{u} , \hat{i} or $\hat{p} = \hat{i} \cdot \hat{u}$). The second contains the corresponding time depending angle $\gamma = 2\pi f t$ as well as the phase shift $\varphi = \angle \underline{i} \underline{u}$ of the variable.

TABLE I. ARM POWER ANALYSIS

No.	u	i	$p_{c,0}$	$\underline{p}_c = p_{c,\alpha} + jp_{c,\beta}$
1	\hat{u}_o	\hat{i}_o	$-1/2 \hat{i}_o \hat{u}_o$	$-1/2 \hat{i}_o \hat{u}_o$
	γ_o	$\gamma_o - \varphi_o$	φ_o	$-2 \gamma_o + \varphi_o$
2	\hat{u}_o	$\hat{i}_{m,P}$	$1/2 \hat{i}_{m,P} \hat{u}_o$	$1/2 \hat{i}_{m,P} \hat{u}_o$
	γ_o	$\gamma_o - \varphi_o$	φ_o	$-2 \gamma_o + \varphi_o$
3	\hat{u}_o	$\hat{i}_{m,N}$	$1/2 \hat{i}_{m,N} \hat{u}_o$	$1/2 \hat{i}_{m,N} \hat{u}_o$
	γ_o	$-\gamma_o - \varphi_{m,N}$	$2 \gamma_o + \varphi_{m,N}$	$\varphi_{m,N}$
4	\hat{u}_o	$\hat{i}_{m,c,0}$	$1/2 \hat{i}_{m,c,0} \hat{u}_o$	$1/2 \hat{i}_{m,c,0} \hat{u}_o$
	γ_o	$\gamma_{c,0} - \varphi_{c,0}$	$\gamma_o - \gamma_{c,0} + \varphi_{m,c,0}$	$-\gamma_{c,0} - \gamma_o + \varphi_{m,c,0}$
5	\hat{u}_{N0}	\hat{i}_o		$-1/2 \hat{i}_o \hat{u}_{c,0}$ $-1/2 \hat{i}_o \hat{u}_{c,0}$
	$\gamma_{c,0}$	$\gamma_o - \varphi_o$		$-\gamma_{c,0} - \gamma_o + \varphi_o$ $\gamma_{c,0} - \gamma_o + \varphi_o$
6	\hat{u}_{N0}	$\hat{i}_{m,P}$		$1/2 \hat{i}_{m,P} \hat{u}_{c,0}$ $1/2 \hat{i}_{m,P} \hat{u}_{c,0}$
	$\gamma_{c,0}$	$\gamma_o - \varphi_o$		$-\gamma_{c,0} - \gamma_o + \varphi_o$ $\gamma_{c,0} - \gamma_o + \varphi_o$
7	\hat{u}_{N0}	$\hat{i}_{m,N}$		$1/2 \hat{i}_{m,N} \hat{u}_{c,0}$ $1/2 \hat{i}_{m,N} \hat{u}_{c,0}$
	$\gamma_{c,0}$	$-\gamma_o - \varphi_{m,N}$		$\gamma_{c,0} + \gamma_o + \varphi_{m,N}$ $\gamma_o - \gamma_{c,0} + \varphi_{m,N}$
8	\hat{u}_{N0}	$\hat{i}_{m,c,0}$		$1/2 \hat{i}_{m,c,0} \hat{u}_{c,0}$ $1/2 \hat{i}_{m,c,0} \hat{u}_{c,0}$
	$\gamma_{c,0}$	$\gamma_{c,0} - \varphi_{m,c,0}$		$-2 \gamma_{c,0} + \varphi_{m,c,0}$ $\varphi_{m,c,0}$

Each of the eight rows of Table I is now searched for active power components. Active power components don't contain a time depending angle γ in the second entry but solely a phase shift φ . Uninfluenceable active power components are marked red. They are formed exclusively from disturbance variables that cannot be influenced (output voltage \underline{u}_o , output current \underline{i}_o , output angle γ_o and phase shift φ_o). Active power components that can be influenced are marked green. They are formed from at least one free-adjustable variable (CU/CHB common mode voltage $u_{c,0}$ and/or one of the three MPS current components $\underline{i}_{m,P}$, $\underline{i}_{m,N}$ or $\underline{i}_{m,c0}$). All other power components with an angle γ in the second entry are oscillating reactive power components. Since they only cause pulsation of the energies, they are not considered further in the following.

The active power component

$$p_{c,0,R1} = \frac{1}{2} \hat{i}_o \hat{u}_o \cos(\varphi_o) \quad (22)$$

in row No. 1 is the only power component in the $p_{c,0}$ column (index "R1"= row No. 1) which cannot be influenced.

$$p_{c,0,R2} = \frac{1}{2} \hat{i}_{m,P} \hat{u}_o \cos(\varphi_o) \quad (23)$$

The active power component in row No. 2 is the only power component in the $p_{c,0}$ column, which can be influenced. Thus the $p_{c,0,R2}$ has to compensate $p_{c,0,R1}$ and also has to be used to balance the mean energy $w_{c,0}$. To balance the difference energies $w_{c,\alpha\beta}$ the active power component

$$p_{c,R3} = \frac{1}{2} \hat{i}_{m,N} \hat{u}_o (\cos(\varphi_{m,N}) + j \sin(\varphi_{m,N})) \quad (24)$$

in row No. 3 or the active power component

$$p_{c,R8} = \frac{1}{2} \hat{i}_{m,c0} \hat{u}_{c,0} (\cos(\varphi_{c,0}) + j \sin(\varphi_{c,0})) \quad (25)$$

in row No. 8 have to be used.

In the next step the reference values for the control variables ($\underline{i}_{m,P}$, $\underline{i}_{m,N}$, $\underline{i}_{m,c0}$ and $u_{c,0}$) are derived from (22)-(25), the vector rotation matrix $[D(\gamma)]$ from (26) and the power reference values ($p_{c,0}^*$, $p_{c,\alpha}^*$ and $p_{c,\beta}^*$).

$$[D(\gamma)] = \begin{bmatrix} \cos(\gamma) & \sin(\gamma) \\ -\sin(\gamma) & \cos(\gamma) \end{bmatrix} \quad (26)$$

The mean energy $w_{c,0}$ is controlled over the entire frequency range $-f_{\max} < f_o < f_{\max}$ with the reference currents $i_{pc0,\alpha\beta}^*$, which are calculated with (27).

$$\begin{bmatrix} i_{m,P,\alpha} - i_{o,\alpha} \\ i_{m,P,\beta} - i_{o,\beta} \end{bmatrix} = \begin{bmatrix} i_{pc0,\alpha}^* \\ i_{pc0,\beta}^* \end{bmatrix} = \frac{2}{\hat{u}_o} [D(\gamma_o)] \begin{bmatrix} p_{c,0}^* \\ 0 \end{bmatrix} \quad (27)$$

For output frequencies f_o above the low frequency f_{LF} threshold ($|f_o| \geq |f_{LF}|$) the difference energies $w_{c,\alpha\beta}$ are controlled via the reference currents $i_{pc,HF,\alpha\beta}^*$ of the negativ current sequence calculated with (28).

$$\begin{bmatrix} i_{m,N,\alpha} \\ i_{m,N,\beta} \end{bmatrix} = \begin{bmatrix} i_{pc,HF,\alpha}^* \\ i_{pc,HF,\beta}^* \end{bmatrix} = \frac{2}{\hat{u}_o} [D(-\gamma_o)] \begin{bmatrix} p_{c,\alpha}^* \\ -p_{c,\beta}^* \end{bmatrix} \quad (28)$$

Taking (14) and the reactive power components marked orange in rows No. 1-3 of Table I into account, it can be seen that the pulsation of the energies $w_{c,0}$ and $w_{c,\alpha\beta}$ is increasing at low output frequencies $|f_o| < |f_{LF}|$. At frequency $f_o = 0$ the oscillating reactive power components become active power components. Therefore, for frequencies $|f_o| < |f_{LF}|$ the difference energies $w_{c,\alpha\beta}$ are not controlled with the negativ current sequence ($i_{pc,HF,\alpha\beta}^*(|f_o| < |f_{LF}|) = 0$). Instead, the high-frequency ($f_{c,0} \gg |f_{LF}|$) common mode voltage $u_{c,0}^*$ and the corresponding positive current sequence $i_{pc,LF,\alpha\beta}^*$ of (29) are used to control the difference energies.

$$\begin{bmatrix} i_{m,c0,\alpha} \\ i_{m,c0,\beta} \end{bmatrix} = \begin{bmatrix} i_{pc,LF,\alpha}^* \\ i_{pc,LF,\beta}^* \end{bmatrix} = \frac{2}{\hat{u}_{c,0}} [D(\gamma_{c,0})] \begin{bmatrix} p_{c,\alpha}^* \\ p_{c,\beta}^* \end{bmatrix} \quad (29)$$

This type of difference energy control is not used over the entire frequency range as it requires a higher voltage reserve of the CU/CHB ($i_{pc,LF,\alpha\beta}^*(|f_o| > |f_{LF}|) = 0 = u_{c,0}^*(|f_o| > |f_{LF}|)$). Furthermore the common mode voltage amplitude $\hat{u}_{c,0}$ calculated with (30) is usually lower than the output voltage amplitude \hat{u}_o , whereas $u_{c,C123,\min}$ is the minimal allowed arm capacitor voltage. Therefore, the difference energy control with $u_{c,0}$ leads to a higher current load on the CU/CHB.

$$\hat{u}_{c,0} = u_{c,C123,\min} - \hat{u}_o \quad (30)$$

Finally the overall current reference value for the current controller is calculated with (31).

$$\begin{bmatrix} i_{c,\alpha}^* \\ i_{c,\beta}^* \end{bmatrix} = \begin{bmatrix} i_{pc0,\alpha}^* \\ i_{pc0,\beta}^* \end{bmatrix} + \begin{bmatrix} i_{pc,HF,\alpha}^* \\ i_{pc,HF,\beta}^* \end{bmatrix} + \begin{bmatrix} i_{pc,LF,\alpha}^* \\ i_{pc,LF,\beta}^* \end{bmatrix} \quad (31)$$

III. CASCADED CONTROL SCHEME

In Fig. 4 the cascaded control scheme is presented. It is derived from the power analysis in Section II.B. First, the arm energy values $w_{c,x}$ and $w_{c,x}^*$ are calculated from the measured values

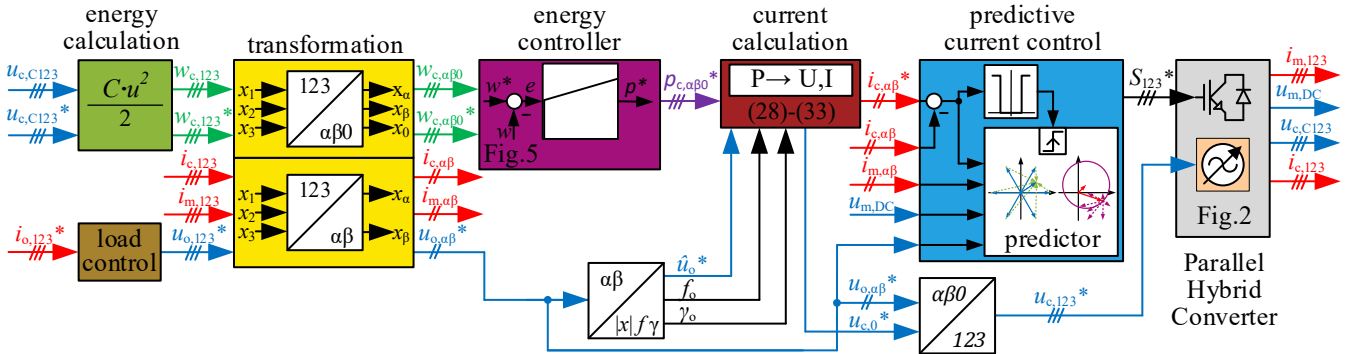


Fig. 4 Energy and Current Control Scheme of the PHC

and the reference values of the arm capacitor voltages $u_{c,Cx}$ and $u_{c,Cx}^*$ according to (6). Then the arm energies $w_{c,x}$ and $w_{c,x}^*$, the measured MPS and CU/CHB currents $i_{m,x}$ and $i_{c,x}$ as well as the reference output voltage values $u_{o,x}^*$ are transformed with the Clarke transformation into the $\alpha\beta$ -system. The arm energies are then fed into the energy controller which calculates the requested power reference values $p_{c,0}^*$, $p_{c,\alpha}^*$ and $p_{c,\beta}^*$ to balance each of the three energies ($w_{c,0}$, $w_{c,\alpha}$, $w_{c,\beta}$) separately.

In Fig. 5 the control loop for the energy controller is depicted. The loop consists of a dead time T_d from the subordinated current controller, an integrator with a gain of 1 and the energy controller itself. The energy controller uses a PI-controller and a low pass filter with a cutoff frequency of $1/T_f$ for the measured values. The filter is used to damp high frequent energy pulsations in the feedback loop and thus increase stability. The PI-controller is designed using the symmetrical optimum according to (32)-(34) with

$$T_{\sigma w} = T_d + T_f \quad (32)$$

as the sum of the minor time constants. The proportional gain factor

$$K_p = 1/(T_{\sigma w} \cdot a) \quad (33)$$

and the integral gain factor

$$K_i = 1/(T_{\sigma w}^2 \cdot a^3) \quad (34)$$

are calculated with the damping factor of the closed loop control being $a = 2$ [10]. To ensure a symmetric energy distribution to the three CU/CHB arms, the reference values for the energy controller are $w_{c,0}^* = \bar{w}_c$ for the mean energy $w_{c,0}$ and $w_{c,\alpha\beta}^* = 0$ for the difference energies $w_{c,\alpha\beta}$.

Then in Fig. 4 the current calculation block is fed with the power reference values $p_{c,\alpha\beta}^*$, the PHC output voltage amplitude reference value \hat{u}_o^* , frequency f_o and angle γ_o . In this block the powers reference values $p_{c,\alpha\beta}^*$ are converted to the reference values for the CU/CHB currents $i_{c,\alpha\beta}^*$ and the CU/CHB common mode voltage $u_{c,0}^*$. Therefore, the equations (26)-(31) derived from the power analysis performed in Section II.B are used.

In the next step the CU/CHB reference current values $i_{c,\alpha\beta}^*$ are fed to the current controller. The current controller determines the three reference switching states

$$\begin{bmatrix} S_1^* \\ S_2^* \\ S_3^* \end{bmatrix} \in \left\{ \begin{bmatrix} 1 \\ 0 \\ 0 \end{bmatrix}, \begin{bmatrix} 1 \\ 1 \\ 0 \end{bmatrix}, \begin{bmatrix} 0 \\ 1 \\ 1 \end{bmatrix}, \begin{bmatrix} 0 \\ 0 \\ 1 \end{bmatrix}, \begin{bmatrix} 1 \\ 0 \\ 1 \end{bmatrix}, \begin{bmatrix} 1 \\ 1 \\ 1 \end{bmatrix}, \begin{bmatrix} 0 \\ 1 \\ 0 \end{bmatrix} \right\} \quad (35)$$

of the three half bridges of the MPS. Where the state $S_x^* = 1$ indicates that the top side IGBT T_x is on and the bottom side IGBT B_x is off and for $S_x^* = 0$ vice versa. The current controller has to select the MPS switching states S_{123}^* in order to fulfil the following goals:

1. ensure that the CU/CHB actual currents \underline{i}_c correspond to the current reference values \underline{i}_c^* on average and thus balance the CU/CHB arm capacitor energies $w_{c,x}$
2. ensure that the MPS current equals the PHC output current $\underline{i}_m \approx \underline{i}_o$ on average, since the CU/CHB has no power source on its own

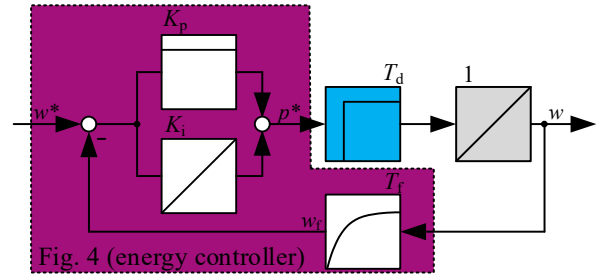


Fig. 5 Control loop of the energy controller

3. limit the MPS current ripples, which flow into the CU/CHB
4. achieve goal 1 and 3 with a minimum number of switching operations within the MPS

Thus a limit controller with a high sampling rate but a low effective switching frequency has to be used. In this paper we decided to adapt and modify the Predictive Current Controller (PCC) presented in [11] to fulfil the above required goals.

In Fig. 6 a drawn example of the current trajectory prediction of the PCC is illustrated. The modified PCC algorithm calculates the current error trajectory

$$\underline{e}_c = \underline{i}_c - \underline{i}_c^* \quad (36)$$

in the $\alpha\beta$ -system between the actual and the reference value of the CU/CHB current. The calculation is done with the high sample rate frequency $f_{PCC,sample}$. Once the error trajectory at time point t_0 reaches the boundary circle, as depicted in the example in Fig. 6 b), the predictor is activated ((37)).

$$|e_c(t_0)| \geq e_{c,max} \quad (37)$$

The predictor then calculates with (38) on basis of the equivalent circuit diagram from Fig. 3 a) the voltage space vector $\underline{u}_{Lm,k}$ of the coupling inductors L_m for all eight possible switching states $S_{123,k}$, see Fig. 6 a). The index $k \in \{1,2,3,4,5,6,7,8\}$ defines the switching state number.

$$\underline{u}_{Lm,k} = \underline{u}_{m,k} - \underline{u}_c^* - R_m \underline{i}_m \quad (38)$$

With $\underline{u}_{Lm,k}$ and L_m the eight possible changes of the MPS currents $d\underline{i}_{m,k}/dt$ could be calculated. In the following we assume that the CU/CHB voltage \underline{u}_c^* does not change between two boundary circle violation events. Thus we can assume firstly the change in the MPS current is linear and secondly according to Fig. 3 c), the output current \underline{i}_o does not change. Considering (10) and (36) we can therefore assume that (39) applies and the error trajectories $\underline{e}_{c,k}$ change linear.

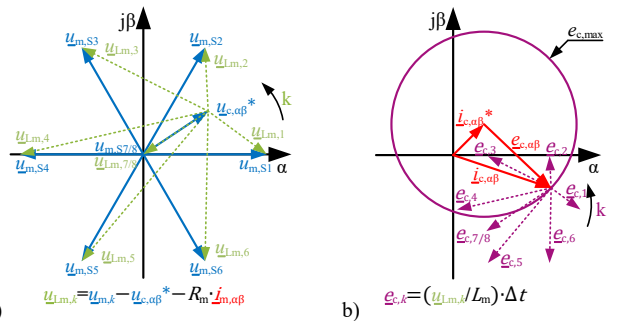


Fig. 6 Voltage (left) and current (right) space vectors for the PCC algorithm with current error boundary circle

$$\frac{de_{c,k}}{dt} = \frac{di_{m,k}}{dt} = \frac{u_{Lm,k}}{L_m} \quad (39)$$

Thus the paths of the eight possible error trajectories $e_{c,k}$ can be interpolated linearly with (40). Fig. 6 b) shows the paths of the error trajectories $e_{c,k}$ as dotted purple arrows for a certain time step Δt .

$$e_{c,k}(t_0 + \Delta t) = e_c(t_0) + \frac{de_{c,k}}{dt} \Delta t \quad (40)$$

Then the time values Δt_k until the error trajectories $e_{c,k}$ reach the boundary circle again are calculated for all possible switching states $S_{123,k}$ with (41) [11].

$$\Delta t_k = - \left(2e_c \frac{de_{c,k}}{dt} \right) / \left(\frac{de_{c,k}}{dt} \right)^2 \cdot \frac{1}{n_k} \quad (41)$$

Thereby the time values are weighted with their corresponding sum of switching operations n_k calculated with (42).

$$n_k = \begin{cases} \sum_{x=1}^3 |S_x - S_{x,k}| & \text{for } S_{123,old} \neq S_{123,k} \\ 1 & \text{for } S_{123,old} = S_{123,k} \end{cases} \quad (42)$$

Only if the value of Δt_k is positive, the corresponding error trajectory $e_{c,k}$ leads back into the boundary circle. At last the next switching state $S_{123,next}$ is determined by looking for the maximum value of all eight Δt_k and selecting the corresponding switching state $S_{123,k}$. Thus the PCC ensures that i_c correspond on average to i_c^* and that the superimposed MPS current ripples are limited to the value of the boundary circle radius $e_{c,max}$. In return, this ensures according to (10) that the MPS delivers the PHC output current i_o on average.

Finally the selected switching state $S_{123,next}$ is fed to MPS IGBTs and the back transformed CU/CHB voltage reference values $u_{c,123}^*$ are sent to a modulator which balances and selects the according cells in the three CU/CHB arms.

IV. SIMULATION

In this Section simulation results of the proposed Cascaded-H-Bridge based Parallel Hybrid Converter using MATLAB/SIMULINK with PLECS BLOCKSET are presented. The parameters used in the simulation are given in Table II. Fig. 7 shows the simulation results for a frequency sweep from -1000 Hz to 1000 Hz (see Fig. 7 h)). On the left the entire frequency sweep and on the right the last 0.5 ms of the simulation are shown. The output voltage amplitude reference value is chosen to $\hat{u}_o^* = 325$ V. The output is connected to an ohmic-inductive three-phase load with the resistor R_o and the inductance L_o . Fig. 7 a) and b) show the PHC output voltages $u_{o,x}$ and currents $i_{o,x}$. The PHC output has the same typical sinusoidal and low-distortion output characteristic as known multilevel converter topologies such as the MMC or MPPMC. As expected, the MPS voltages $u_{m,x}$ shown in Fig. 7 c) are only two level voltages in comparison and the resulting MPS currents $i_{m,x}$ shown in Fig. 7 d) have high current ripple. The average switching frequency of the MPS IGBTs in the simulation is $\bar{f}_{m,sw} \approx 9$ kHz. Fig. 7 e) shows the sinusoidal multilevel CU/CHB voltages $u_{c,x}$ with the high frequency common mode voltage $u_{c,0}$ in the range of $|f_o| < |f_{LF}|$. As described in this

TABLE II. SIMULATION PARAMETERS

Symbol	Value	Description
$u_{m,DC}$	700 V	MPS DC-link voltage
L_m	200 μ H	coupling inductances
R_m	20 m Ω	line resistances of L_M
N	8	number of cells per arm
$C_{c,xy}$	567.2 μ F	cell capacitance
$u_{c,Cxy}^*$	60 V	cell capacitor voltage reference value
$C_{c,x}$	70.9 μ F	arm capacitance
$u_{c,Cx}^*$	480 V	arm capacitor voltage reference value
f_{LF}	20 Hz	low frequency threshold
$1/T_f$	50 Hz	energy controller feedback filter cutoff frequency
$f_{c,sw}$	50 kHz	CU/CHB PWM and control frequency
$f_{PCC,sample}$	500 kHz	sampling frequency of the PCC
\hat{u}_o^*	325 V	output voltage amplitude
L_o	100 μ H	load inductances
R_o	3.25 Ω	load resistances

paper ((4)) and depicted in Fig. 7 f) the CU/CHB currents $i_{c,x}$ are composed only from the difference between the high fidelity output currents and the highly rippled MPS currents. The RMS values of the MPS, the PHC output and the CU/CHB currents in the last 0.5 ms are $i_{m,RMS} = 70.46$ A, $i_{o,RMS} = 69.37$ A and $i_{c,RMS} = 8.12$ A. The current rating of the CU/CHB must therefore only be ~ 12 % of the MPS current rating. This shows that with the PHC we present a new converter topology with significant reduced costs and a significant improved power density compared to conventional multilevel converter topologies such as MMCs or MPPMCs. At last Fig. 7 g) shows that the derived control scheme balances the arm capacitor voltages $u_{c,Cx}$ of the CU/CHB very precisely over the entire frequency range also for DC output voltage.

V. CONCLUSION

In this paper we present and analyze the new ‘‘Parallel Hybrid Converter’’ (PHC) topology. The PHC topology combines a low power Cascaded-H-Bridge Converter (CHB) as ‘‘Correction Unit’’ (CU) with a high power two level IGBT converter as ‘‘Main Power Source’’ (MPS) in a parallel arrangement. This new converter topology is perfectly suited to be used as a universal low harmonics sinusoidal voltage source and can replace single high power and expensive multilevel converters such as a Modular Multilevel Converter (MMC) or a Modular Multiphase Multilevel Converter (MPPMC). In order to ensure a precise balancing of the CU/CHB cell capacitor energies we derived a decoupled control scheme. Superimposed PI controllers balancing the capacitor energies determine the transformed arm power reference values. With the results of a performed arm power analysis, the power reference values are converted to current reference values. The current reference values are fed to a Predictive Current Controller (PCC). The PCC determines the switching states of the MPS IGBTs and therefore limits the CU/CHB currents and controls the MPS currents. The simulation results show that the PHC has a terminal behavior similar to a MMC or MPPMC but compared to them the PHC allows significant reduction in costs and a significant increase in power density. The simulation also shows that the derived control scheme precisely balances the CU/CHB cell capacitor energies. A 50 kW prototype is under construction and will be used for Power-Hardware-in-the-Loop (PHIL) Emulation of electrical machines and small power grids.

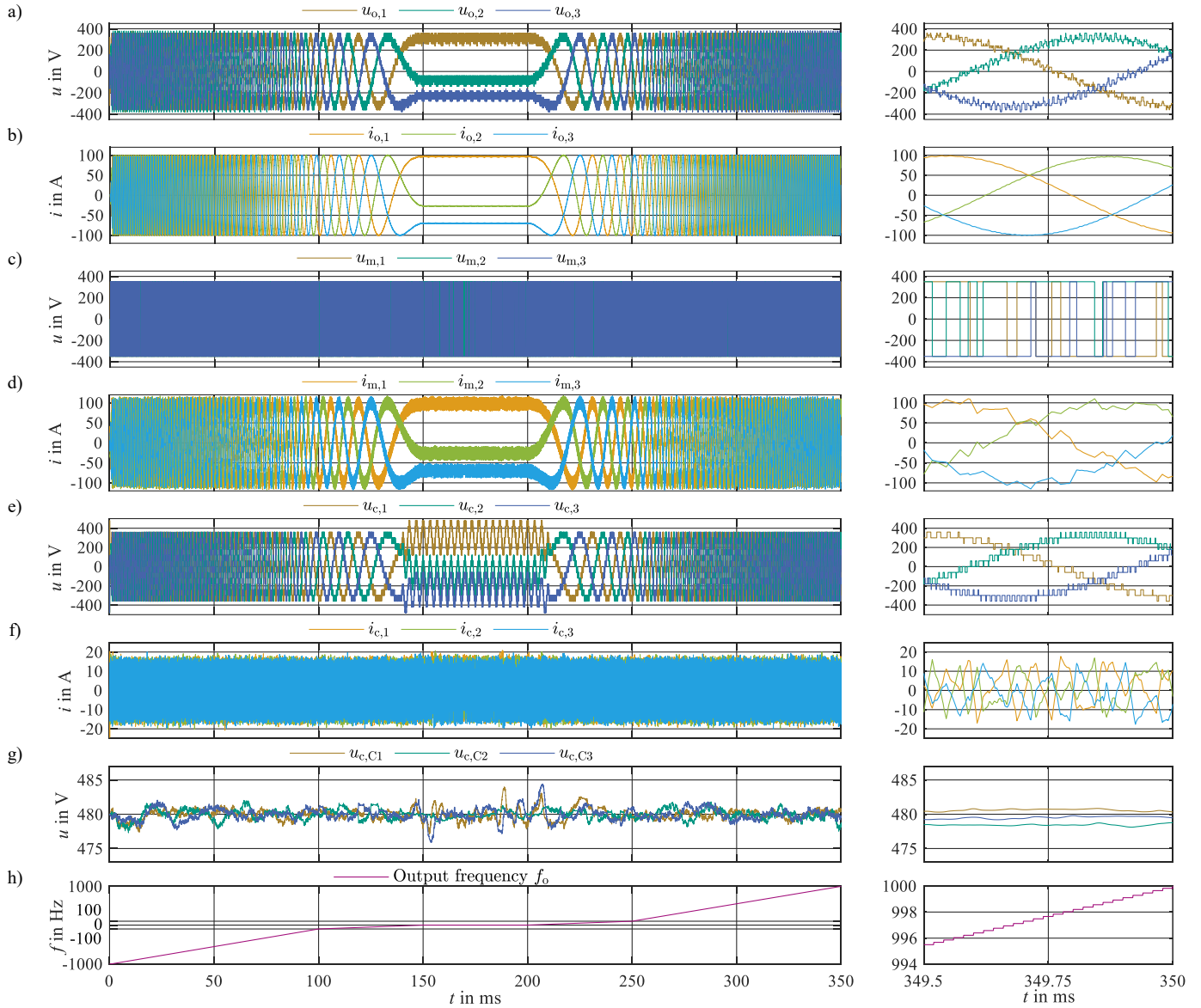


Fig. 7 Simulation results of the PHC with the proposed control concept with an frequency sweep from -1000 Hz to 1000 Hz . On the left the entire frequency sweep and on the right the last 0.5 ms of the simulation are shown. The reference value of the output voltage amplitude is chosen to be $\hat{u}_o^* = 325\text{ V}$.

REFERENCES

- [1] G. B. Yundt, "Series Parallel Connected Composite Amplifiers," M.Sc. Thesis, Massachusetts Institute of Technology, Boston, 1983.
- [2] H. Ertl, J. W. Kolar, F. C. Zach, "A New 1kW Class-D Supported Linear Power Amplifier Employing a Self-Adjusting Ripple Cancellation Scheme," in *Proceedings of the 29th International Conference on Power Conversion (PCIM 1996)*, Nuremberg, Germany, 1996, pp. 265-274.
- [3] H. Ertl, J. W. Kolar, and F. C. Zach, "Basic considerations and topologies of switched-mode assisted linear power amplifiers," *IEEE Transactions on Industrial Electronics*, vol. 44, no. 1, pp. 116-123, 1997.
- [4] G. B. Yundt, "Series- or Parallel-Connected Composite Amplifiers," *IEEE Transactions on Power Electronics*, vol. PE-1, no. 1, pp. 48-54, 1986.
- [5] M. Schnarrenberger, F. Kammerer, M. Gommeringer, J. Kolb, and M. Braun, "Current control and energy balancing of a square-wave powered 1AC-3AC modular multilevel converter," in *2015 IEEE Energy Conversion Congress and Exposition (ECCE)*, 2015, pp. 3607-3614.
- [6] A. Schmitt, M. Gommeringer, J. Kolb, and M. Braun, "A High Current, High Frequency Modular Multiphase Multilevel Converter for Power Hardware-in-the-Loop Emulation," in *PCIM Europe 2014*, Nuremberg, Germany: VDE, 2014, pp. 1537-1544.
- [7] D. Bernet, L. Stefanski, R. Schwendemann, C. Rollbuhler, and M. Hiller, "Grid-Connected Voltage Source Converters with integrated Multilevel-Based Active Filters," in *2018 IEEE Energy Conversion Congress and Exposition (ECCE)*, Portland, OR, pp. 127-134.
- [8] D. Bernet, L. Stefanski, and M. Hiller, "A Hybrid Medium Voltage Multilevel Converter with Parallel Voltage-Source Active Filter," in *10th International Conference on Power Electronics-(ECCE Asia)*, Busan, Korea, May. 2019, pp. 412-419.
- [9] J. Kolb, F. Kammerer, M. Gommeringer, and M. Braun, "Cascaded Control System of the Modular Multilevel Converter for Feeding Variable-Speed Drives," *IEEE Trans. Power Electron.*, vol. 30, no. 1, pp. 349-357, 2015.
- [10] D. Schröder, *Elektrische Antriebe - Regelung von Antriebssystemen*. Berlin, Heidelberg: Springer Berlin Heidelberg, 2015.
- [11] J. Holtz, "Advanced PWM and Predictive Control—An Overview," *IEEE Trans. Ind. Electron.*, vol. 63, no. 6, pp. 3837-3844, 2016.